

AN EXAMINATION OF GALACTIC POLARIZATION WITH APPLICATION TO THE PLANCK TB CORRELATION

J. L. WEILAND, G. E. ADDISON, C. L. BENNETT

Department of Physics and Astronomy, Johns Hopkins University, 3400 N. Charles St, Baltimore, MD 21218, USA

AND

M. HALPERN, G. HINSHAW

Department of Physics and Astronomy, University of British Columbia, Vancouver, BC, V6T 1Z1, Canada

Draft version June 8, 2022

ABSTRACT

Angular power spectra computed from *Planck* HFI 353 GHz intensity and polarization maps produce a *TB* correlation that can be approximated by a power-law (Planck Collaboration XI 2018). Whether the observed *TB* correlation is an induced systematic feature or a physical property of Galactic dust emission is of interest both for cosmological and Galactic studies. We investigate the large angular scale *E* and *B*-mode morphology of microwave polarized thermal dust emission, and relate it to physical quantities of polarization angle and polarization fraction. We use empirical models of polarized dust to show that dust polarization angle is a key factor in producing the *TB* correlation. A small sample of both simulated and observed polarization angle maps are combined with 353 GHz intensity and dust polarization fraction to produce a suite of maps from which we compute *TB* and *EB*. Model realizations that produce a positive *TB* correlation are common and can result from large-scale ($> 5^\circ$) structure in the polarization angle. The *TB* correlation appears robust to introduction of individual intensity, polarization angle and polarization fraction model components that are independent of the 353 GHz observations. We conclude that the observed *TB* correlation is likely the result of large-scale Galactic dust polarization properties.

1. INTRODUCTION

Cosmic Microwave Background (CMB) research is currently focused toward obtaining high sensitivity observations of the polarized CMB, as characterized by divergence free *B*-modes and curl-free *E*-modes (Zaldarriaga & Seljak 1997; Kamionkowski et al. 1997). *B*-modes are sensitive to the imprint of primordial gravitational waves sourced by inflation with an amplitude denoted by the tensor-to-scalar ratio parameter, r . Detection of these inflationary *B*-modes would constrain the energy scales of inflation and provide unique insight into the early universe. *E*-modes observed on large spatial scales provide a direct constraint on the reionization optical depth parameter τ , and are important for cosmological neutrino mass constraints (e.g., Allison et al. 2015). Current and upcoming experiments are targeting high multipole (up to $l \simeq 3000 - 5000$) polarization measurements to more stringently test the Λ CDM model and provide tighter constraints on the gravitational lensing of the CMB by large-scale structure (e.g., Benson et al. 2014; Henderson et al. 2016; Ade et al. 2019).

Because the signal from the polarized CMB is subdominant to the Milky Way’s polarized foreground emission, it has become increasingly important to both quantify and understand these foregrounds. At microwave frequencies, the two significant emission mechanisms are synchrotron and thermal dust emission (Page et al. 2007; Bennett et al. 2013; Planck Collaboration X 2016; Planck Collaboration IV 2018). The polarized foregrounds are usually observed and characterized in terms of the Stokes parameters: I , Q , U , and V , but of primary interest are the

linear polarization parameters Q and U . While Stokes Q and U are observationally convenient, they are coordinate system dependent so they do not couple naturally to the underlying physics. For this, the *E*-mode and *B*-mode representation of orthogonal polarization components is ideal. Despite this, sky maps are usually shown in Q and U and foreground masking is generally implemented for Q and U maps before transforming and computing *E* and *B* power spectra.

A relatively recent foreground-related puzzle originates with analysis of *Planck* HFI data, where the dominant polarized foreground is that from thermal dust emission. Angular power spectra computed from HFI 353 GHz intensity¹ and polarization maps show a significant positive signal in the Temperature *B*-mode (*TB*) cross spectrum, but an *EB* cross spectrum consistent with zero signal (Planck Collaboration XI 2018; Planck Collaboration Int. LIV 2018; Planck Collaboration Int. XXX 2016). The *TB* spectrum is roughly consistent with a power law as a function of multipole moment l for $l \lesssim 600$, although there is significant scatter in the data points about the fit. We refer to this characteristic as “non-zero *TB*” throughout this paper. Physical arguments predict the *TB* and *EB* signals from the CMB to be statistically consistent with zero (e.g., Zaldarriaga & Seljak 1997). Thus the two most likely sources for the non-zero *TB* signal are residual systematics in the data, and/or a non-zero *TB* contribution from Galactic thermal dust emission.

The reported detection of a non-zero *TB* signal in the HFI 353 GHz data is a finding of interest regardless of

¹ When expressed in temperature units, the intensity map I is often referred to as “the temperature map”, or T .

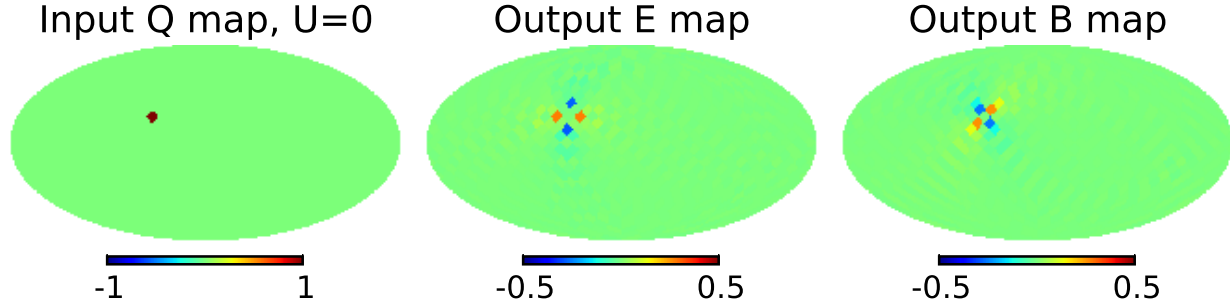


Figure 1. Illustration of how a single pixel with Stokes parameters $Q = 1$, $U = 0$ (left) transforms into E (middle) and B (right). The transform distributes signal from a single pixel in $[Q, U]$ over multiple pixels in E and B . Note the change in color scale between Q and the E and B maps. Other examples involving multiple pixels can show less localized power redistribution. As a consequence of the pixel redistribution, masks appropriate to Stokes Q and U maps are not directly applicable to the their associated E and B maps, and mapping of Q and U features into E and B is not completely intuitive.

its origin, but carries different ramifications depending on the source of that signal. If the TB signal arises from Galactic emission processes, it has implications for magnetic field structure studies and for CMB experiments. Calibration of CMB observations may rely on hardware, astrophysical sources, and/or use “self-calibration”, in which assumptions of null EB and sometimes TB spectra define the detector polarization angles and indicate the presence of potential measurement systematics (e.g., Kaufman et al. 2014; Koopman et al. 2016). Characterization of a non-zero TB sky signal would be essential knowledge for self-calibration. Efforts to find physical mechanisms to reproduce the *Planck* TB correlation are ongoing; the model of Huffenberger et al. (2019) predicts both positive TB and EB (at a lower level) based on alignment of diffuse ISM filaments with that of the Galactic magnetic field orientation. Conversely, if the *Planck* 353 GHz TB signal arises from residual systematics in the data, possible analysis bias in CMB as well as Galactic emission component studies may be introduced through the assumption that these maps are accurate templates of polarized Galactic dust emission.

This paper has two motivations: (1) obtaining some basic insights into the E and B morphology of polarized emission from Galactic foregrounds, and (2) attempting to understand the origin of the non-zero TB signal in *Planck* data. In Section 2, we discuss the $[Q, U]$ to $[E, B]$ transformation, and show observations of polarized synchrotron and dust foregrounds in both representations in order to illustrate relevant spatial features in the E and B maps. The remainder of the analysis discussion (Sections 3, 4 and 5) is devoted to constructing models of Q and U Galactic dust maps assembled from a variety of intensity, polarization fraction and polarization angle map components, and examining how the nature of these components affects both $[E, B]$ and the resultant TB power spectra. Varying individual components within empirical models allows us to test the stability of the observed non-zero TB spectrum. Section 3 presents empirical models in which we examine the role of dust polarization angle and polarization fraction in the spatial structure of the $[E, B]$ maps. In Section 4, we compute TB and EB power spectra of the models from Section 3, relate the origin of the non-zero TB spectrum to the polarization angle, and compute TB spectra for additional models incorporating synthetic polarization angles. We discuss further tests of non-zero TB in Section 5, includ-

ing intensity map variants and the addition of *Planck* 217 GHz polarization data. Section 6 summarizes our conclusions.

2. STOKES $[Q, U]$ AND TRANSFORMATION TO $[E, B]$

E and B may be thought of as complex linear combinations of Stokes Q and U in harmonic space (Zaldarriaga & Seljak 1997; Kamionkowski et al. 1997). In the spatial domain (pixel space), the transformation does not encode all the information from a single Q or U pixel into that same pixel in E and B , but rather distributes the $[Q, U]$ pixel signal across multiple pixels in E and B . As an example, Figure 1 shows the transformation of a single pixel with $Q = 1$, $U = 0$ into E and B maps. The small-scale localized signal in Q transforms into a quadrupolar pattern in E and B : B is rotated 45 degrees with respect to E (Hu & White 1997). The example in the figure uses 3° pixels: the pixel scale sets the size of the $[E, B]$ structure from a single $[Q, U]$ pixel. Signal from larger scale structure transforms in a less localized fashion. Signal redistribution means masks in $[Q, U]$ pixel space do not transform cleanly into E and B . Similarly, convenient foreground characterizations in $[Q, U]$ such as spectral index maps do not transform equivalently into $[E, B]$ as well.

Throughout this paper, we utilize the *healpy*² (Zonca et al. 2019) and *HEALPix*³ (Górski et al. 2005) analysis package. The package function *map2alm* is used to transform Q and U using the spin-2 spherical harmonic basis functions with coefficients a_{lm}^E and a_{lm}^B , and then the function *alm2map* is used to evaluate E and B maps from the a_{lm} ’s. The *healpy* transformation sets monopole and dipole ($l = 0, 1$) components to zero, so that all full-sky $[E, B]$ maps that we show have zero mean and dipole. Additionally, we retain the polarization convention adopted by WMAP and *Planck* data products, which differs from the IAU convention by the sign of Stokes U ⁴.

In Figure 2, we show the temperature (unpolarized intensity) map Stokes I , polarized intensity P ($= [Q^2 + U^2]^{0.5}$), and the transformation from Stokes Q and U to E and B for WMAP K-band (23 GHz) and *Planck* 353 GHz maps. All maps in this paper are shown in

² <https://github.com/healpy/healpy/>

³ <http://healpix.sourceforge.net>

⁴ https://healpix.sourceforge.io/html/intro_HEALPix_conventions.htm

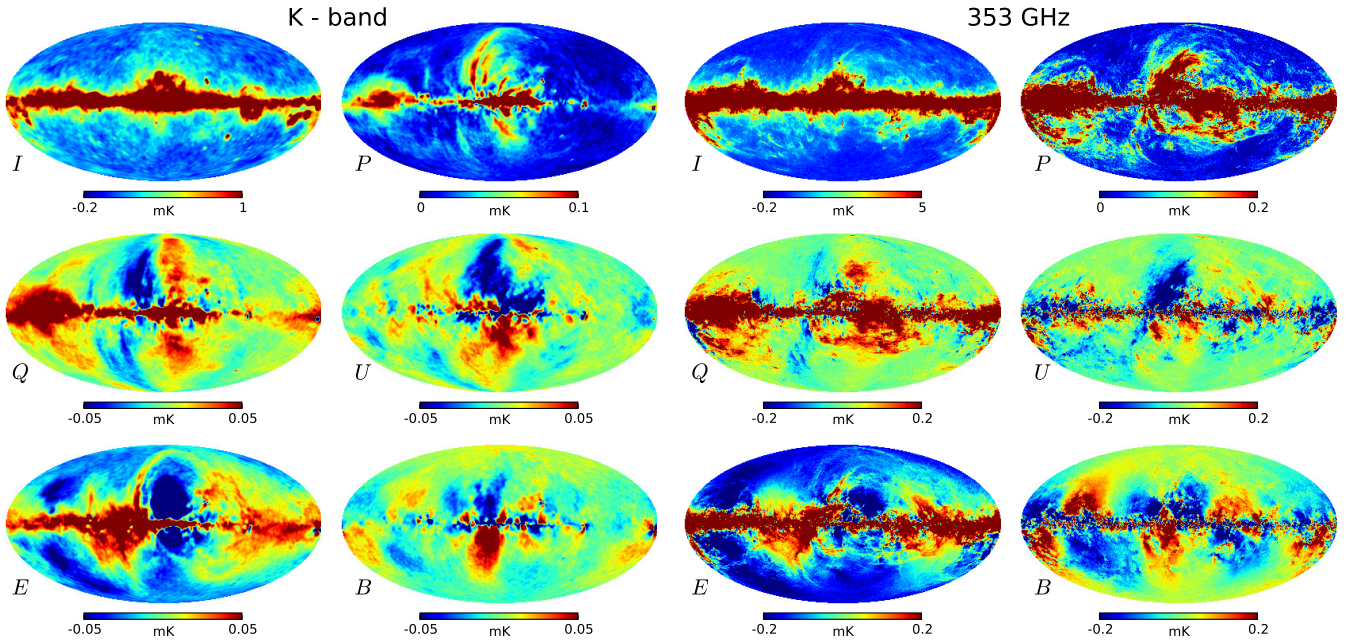


Figure 2. Maps of intensity (I), polarized intensity (P), Stokes $[Q, U]$ and $[E, B]$ for WMAP K-band (23 GHz, 9-year data, left half of plot) and Planck/HFI 353 GHz (2018 data release, right half). Maps have been smoothed in order to reduce visual contamination from instrument noise. We focus on the polarization maps, where the common underlying CMB signal is completely subdominant to the Galactic foreground signals: synchrotron emission in K-band and thermal dust emission at 353 GHz. Although polarized foreground radiation emitters at these two frequencies are both embedded within the same global Galactic magnetic field (GMF), their polarized intensity maps appear quite different from each other (and their intensity maps). The mapping transformation from Stokes $[Q, U]$ to $[E, B]$ offers a different perspective in interpreting the map morphology and dependencies on polarization angle and polarization fraction. In Section 3, we explore in particular the similar large angular scale morphology between the E -mode maps at both frequencies, and strong $l = 3$ signature (positive and negative pattern above and below plane) in the 353 GHz B -mode map.

Galactic coordinates, following astronomical convention, with the Galactic center in the middle. The K-band Q and U maps are dominated by Galactic synchrotron emission and serve as a useful template for that foreground in polarization. Similarly, the 353 GHz Q and U maps may serve as templates describing polarized thermal dust emission. The same unfortunately is not true for the temperature maps, for while the 353 GHz I map is dominated by thermal dust emission outside the Galactic plane, the K-band I map represents a mix of CMB, synchrotron, free-free, and AME (anomalous microwave emission, generally assumed to arise from spinning dust) components. Contributions also arise from point sources and cosmic infrared background asymmetries, but these are not critical to the larger angular scales discussed here. Although we concentrate in this paper on the more easily separable dust emission, we briefly discuss K-band in order to draw certain parallels, since both the synchrotron and dust emission are influenced by the same Galactic magnetic field.

The Galactic plane is clearly visible in all maps of Figure 2, but the details of the structures off the plane are not necessarily physically intuitive, particularly in polarization. The signal from polarized CMB is present in these maps, but is subdominant to Galactic components, such that high Galactic latitude structure at these frequencies represents foreground behavior rather than that of the CMB. The E -mode maps for both K-band and 353 GHz show very similar large-scale structure. The B -mode maps are less alike, with the 353 GHz B -mode map showing a strong contribution from the $l = 3, |m| = 3$ spherical harmonic modes, evidenced as a regular $+/-$ pattern alternating above and below the Galactic plane.

The above figures establish a general overview of the visual appearance of E and B -mode maps for polarized microwave foregrounds. In the next section, we step through some simple models to gain insight into large angular scale E and B map structures.

3. EMPIRICAL MODELS

Stokes Q and U maps may be constructed from an empirical model expressed in terms of a polarization angle γ and polarization fraction f as follows,

$$Q = If \cos(2\gamma) \quad (1)$$

$$U = If \sin(2\gamma) \quad (2)$$

where I is the temperature map, such that $f = P/I$ and $\gamma = 0.5 \tan^{-1}(U, Q)$. We deal with models designed to represent only a single foreground emission component at a given frequency.

The polarization fraction is influenced by a number of factors. For example, a complex line-of-sight column containing multiple emission regions will result in a lower polarization fraction due to the decoherence of preferred directions (e.g., the magnetic field directions) and emission conditions along the column. The polarization angle is influenced by the spiral structure imposed by the global Galactic magnetic field (GMF) and more localized phenomena (e.g., MHD turbulence), and particle-field alignment properties. An observed temperature map I is generally used to provide realistic small-scale information.

In this section, we construct models of $[Q, U]$ in which we vary choices for f and γ , keeping I constant, and note the effect of these individual parameters on the resultant $[E, B]$ spatial structure. We first examine the

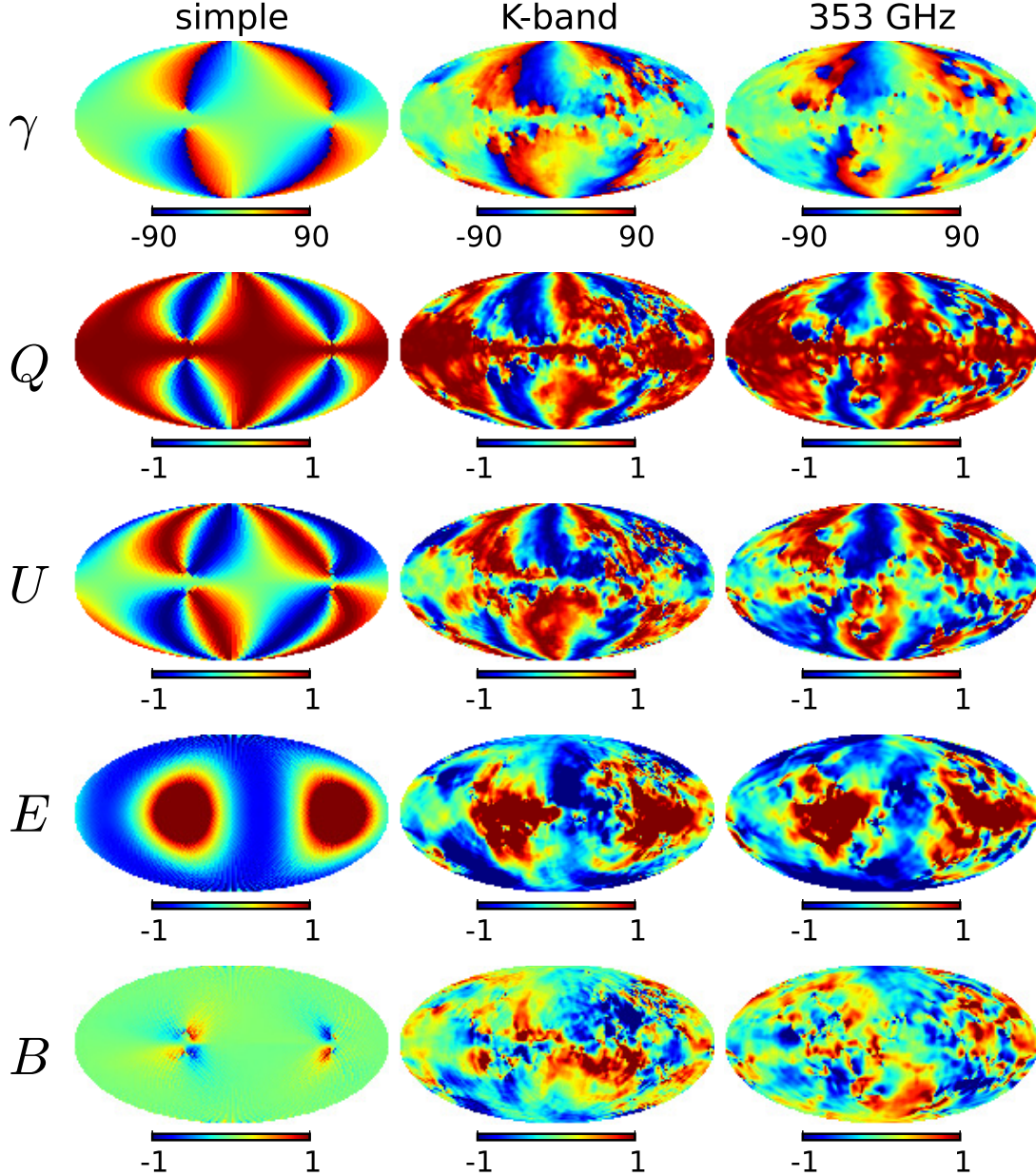


Figure 3. The polarization angle γ determined from Stokes $[Q, U]$ is a coordinate and observer dependent projection of the orientation of the surrounding magnetic field. The large angular scale morphology of the polarization angle is determined by the GMF and emission alignment with that field. We set intensity and polarization fraction to be unity, and show the transformation of three different realizations of γ (first row) into Stokes $[Q, U]$ (next two rows, via $\cos 2\gamma$ and $\sin 2\gamma$) and then into $[E, B]$ (last two rows). Left column: γ corresponding to a simple magnetic field model. Middle column: γ from WMAP K-band $[Q, U]$ maps. Right column: γ from HFI 353 GHz $[Q, U]$ maps. Comparison of the $[Q, U]$ and $[E, B]$ γ maps with the corresponding maps in Figure 2 illustrates the role γ plays in the observed map morphology. The two-lobed large-scale E -mode morphology can be attributed primarily to polarization angle geometry, and thus the GMF. B -mode, however, is not well described by this factor alone.

role that the polarization angle plays in the morphology of the $[Q, U]$ and $[E, B]$ maps, as illustrated in Figure 3. We start with three separate inputs of polarization angle, convert them via eqns 1 and 2 to Q and U maps assuming I and f are everywhere unity over the sky, and then transform those $[Q, U]$ maps to E and B . Two of the three input polarization angle maps are constructed from observations discussed previously: WMAP K-band and Planck 353 GHz Q and U maps, smoothed to 4° FWHM resolution. The third polarization angle example is computed from a simple geometrical model of the GMF (Page et al. 2007). This representation, which we

denote as “simple γ ”, provides a polarization angle map dominated by large angular scale morphology. The polarization angle as observed from the solar neighborhood does not represent the true magnetic field orientation as seen by an outside observer, but is rather a projection. The sign of γ wraps at the directions roughly corresponding the observer’s view looking in both directions down the local Orion arm, roughly at Galactic longitudes 65° and 240° .

We show each of these three polarization angle maps in the top row of Figure 3. The next two rows illustrate the $\cos(2\gamma)$ and $\sin(2\gamma)$ geometrical patterns which heavily

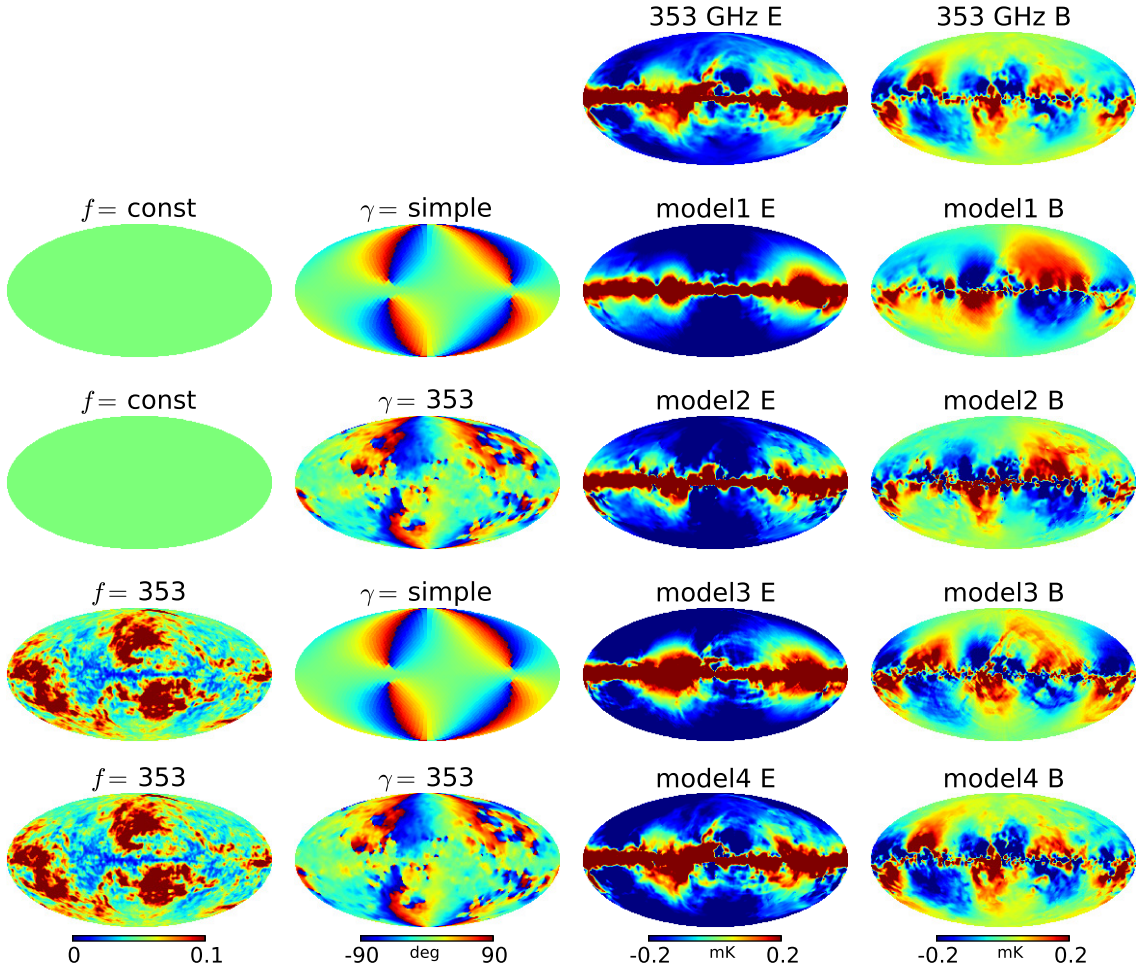


Figure 4. Four empirical models of 353 GHz polarized dust emission are produced from the *Planck* 353 GHz temperature map and two separate variants each of polarization fraction f and polarization angle γ (see equations 1 and 2). The variants of f and γ are chosen to span possible morphologies: f as either spatially constant ($= 0.05$) or a lightly smoothed version derived from *Planck* data, and γ from either a simple GMF or computed from 353 GHz $[Q, U]$. The resultant $[E, B]$ morphologies for each model are shown in rows 2 through 5, for comparison to that of the data (first row). The first and second columns of each model row indicate the choice of f and γ . The third and fourth columns present the $[E, B]$ model maps derived from those parameter choices. As in Figure 3, γ is primarily responsible for the large-scale two-lobed E -mode morphology. Obtaining the strong observed $l = 3$ B -mode, however, requires a polarization fraction morphology similar to that of the 353 GHz data (rows 4 and 5).

influence the appearance of the Q and U maps shown in Figure 2. The E and B -mode maps resulting from these Q and U maps are shown in the fourth and fifth rows respectively. All E -mode maps in this figure show two prominent large-scale emission lobes centered about the viewing directions of the local arm as defined by the GMF orientation. The lobe structure is most obvious in the simple γ E -mode map, but is strongly present both in the $\gamma = \text{K-band}$ and 353 GHz E maps as well. Comparing the E -mode maps derived from the K-band and 353 GHz polarization angle to those of the data in Figure 2, it is clear that much of this large-scale two-lobed structure is attributable to the polarization angle alone.

Comparison of the bottom row of Figure 3 with that of the data make it clear that that the B -mode morphology is not sufficiently explained with polarization angle alone. Having examined the role of γ in $[E, B]$ structure, we now look at the role played by the polarization fraction f via a set of four empirical models shown in Figure 4. The figure concentrates on empirical models of the dust emission at 353 GHz only, because the maps of

I and f for dust are more easily derived than those for K-band synchrotron, as explained earlier. We choose to vary the polarization fraction f between two extremes: a constant $f = 0.05$ over the entire sky, and that produced from a lightly smoothed (0.2°) map of P and I as observed by *Planck*. The P map is produced from *Planck* half-mission maps in order to avoid introducing noise bias. In addition, we choose two bracketing representations of γ : that from the simple geometric GMF model and 353 GHz data shown previously in Figure 3. We permute these f and γ choices with a fixed thermal dust emission temperature map from *Planck* to form the four model combinations. Our versions of γ and f independently derived from 353 GHz data are in good agreement with those shown and discussed in *Planck Collaboration XII (2018)*. We also note that the exact choice of 353 GHz intensity map does not significantly alter our results: for example use of the *Planck* Commander 353 GHz dust map (*Planck Collaboration IV 2018*) rather than the 353 GHz I map produces similar models.

In Figure 4 the E and B maps for the 353 GHz data are shown in the top row and may be compared with the E

and B model maps in the four rows directly below. The two left-most columns specify the f and γ maps used to produce the E and B models shown in each row. On very large scales, the dust B -mode structure takes the form of a quadrupole about the local arm viewing directions near $l = 65^\circ$ and 240° , and expresses itself as a strong $l = 3, |m| = 3$ B -mode pattern about the Galactic plane. The last two rows of the figure illustrate that the specific 353 GHz polarization fraction is necessary to most closely reproduce the observed $l = 3, |m| = 3$ B -mode pattern. There is strong geometrical suppression of the polarization fraction along the spiral arm viewing directions, which is expected because of the complex astrophysics from multiple emission regions along each line-of-sight.

4. TB AND EB SPECTRA OF EMPIRICAL MODELS

We use the four empirical models presented in the previous section to explore which geometrical factors contribute most to producing the non-zero TB signal detected by *Planck*. We construct half-mission Q and U maps using I , f and γ components at *HEALPix* $N_{\text{side}} = 2048$ resolution and evaluate the TB and EB power spectra using *PolSpice*⁵ (Szapudi et al. 2001; Chon et al. 2004). The resultant power spectra are shown in Figure 5. The use of half-mission splits is necessary to avoid noise correlations in the power spectra when generating model components based on the 353 GHz data. Because the I component is always fixed to that of the 353 GHz data, a mask which excludes strong non-dust emission sources present in the data is used. In order to compare our results with that of *Planck Collaboration XI* (2018), we adopt the masking recipe described in *Planck Collaboration XI* (2018) for their analysis mask designated “LR71”. This mask maximizes analyzed sky area while excluding regions of strong CO line emission (primarily near the Galactic plane) and high-latitude polarized point sources above a certain threshold. Due to inexactitudes in the published masking specifications, our mask is slightly different and permits roughly 75% of the sky to be analyzed after apodization (rather than 71%). For visual clarity, power spectra are plotted using multipole bins; the binning ranges are as defined in Table C.1 of *Planck Collaboration XI* (2018). Power spectra are expressed as $D_l = l(l+1)C_l/2\pi$.

The bottom-most plot of Figure 5 shows binned TB (red) and EB (blue) produced from 353 GHz data half-mission cross-spectra, and represents the case where f and γ both arise from 353 GHz data. This image illustrates independent confirmation of the non-zero TB signal and EB spectrum roughly consistent with zero presented in Figure 6 of *Planck Collaboration XI* (2018). *Planck Collaboration XI* (2018) estimate uncertainties for their TB and EB spectra based on analysis of the full-focal plane simulations (FFP10) from the 2018 data release. Similarly, the uncertainties plotted in this panel are derived by applying the same analysis methods to the first 100 FFP10 simulations of noise and dust emission.

The approximate power-law fit derived by *Planck Collaboration XI* (2018) for their LR71 mask is shown in magenta, which we evaluate using their equation 1, $D_l^{TB} = A^{TB}(l/80)^{(\alpha_{TB}+2)}$, with $\alpha_{TB} = -2.44$. The am-

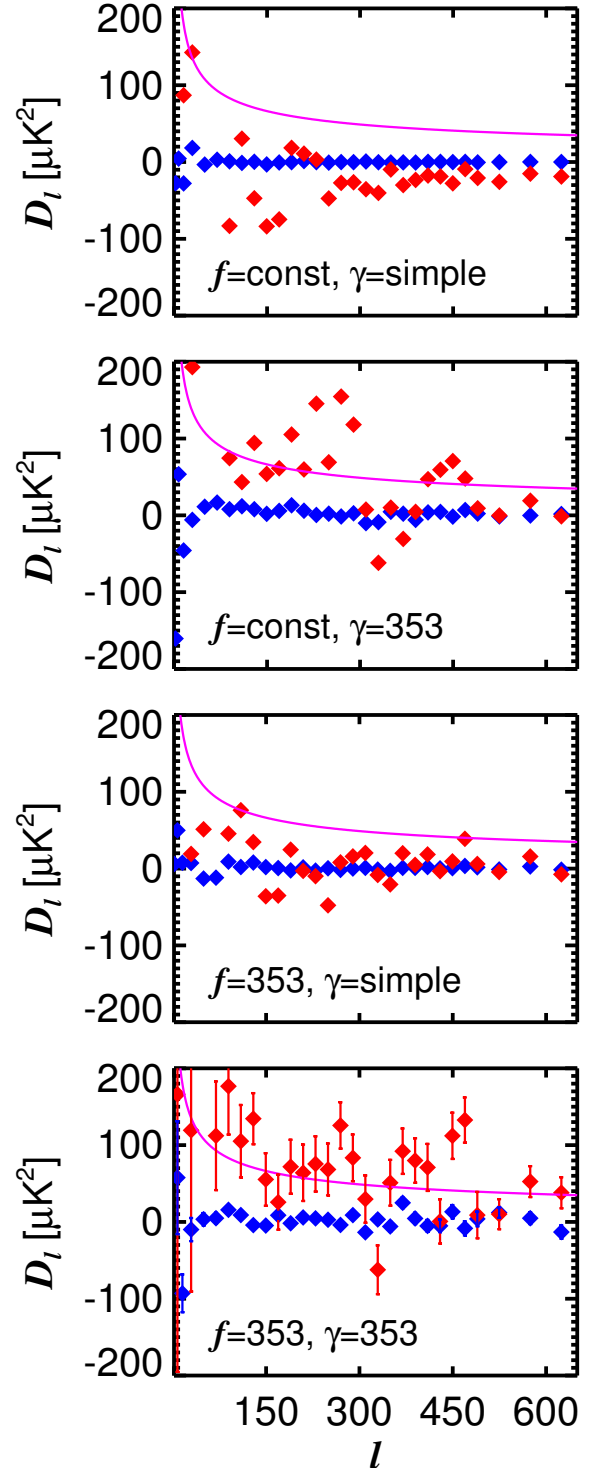


Figure 5. Binned TB (in red) and EB (in blue) power spectra computed for the four empirical models presented in Figure 4, over $\approx 75\%$ of the sky. The magenta line shown in each panel represents the TB power-law fit found by *Planck Collaboration XI* (2018) for their largest sky fraction, and serves as a fiducial level for the observed positive TB signal. Uncertainties estimated from the *Planck* FFP10 noise simulations are overplotted in the last panel; model uncertainties can be expected to be of this magnitude or less because of the reduced noise in some model components. A positive TB signal arises only for the two models formed using a polarization angle based on 353 GHz data. We conclude that origin of the observed non-zero TB signal primarily lies with the γ morphology.

⁵ <http://www2.iap.fr/users/hivon/software/PolSpice/>

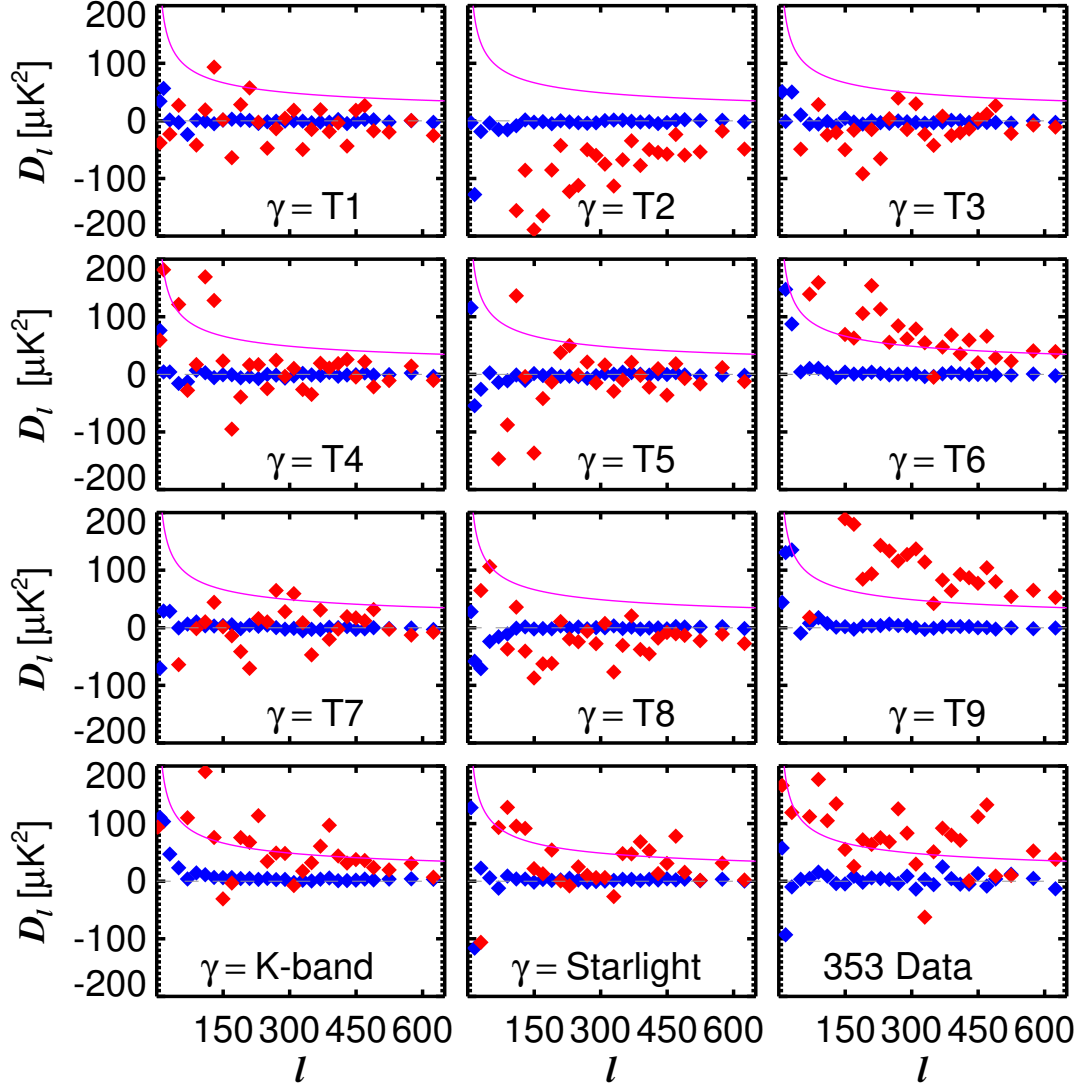


Figure 6. TB (red) and EB (blue) spectra of 353 GHz I , Q and U maps, computed for the 75% mask. All panels, except the lower right (“353 data”), show spectra derived from modeled Q and U realizations. Each realization is constructed from the same set of 353 GHz intensity and polarization fraction maps based on *Planck* data, but each possesses a unique polarization angle morphology. The nine panels labeled with the ‘T1 - T9’ prefix utilize 9 TIGRESS realizations of polarization angle corresponding to different observer locations within the solar neighborhood (see text). Also included are TB and EB spectra for two realizations built using data-based polarization angles which are independent of *Planck* observations. These are shown in the first two panels in the last row, and either use the WMAP K-band polarization angle (‘K-band’), or γ from the polarization of dust by starlight (‘Starlight’, Heiles 2000; Page et al. 2007). The bottom right panel shows the TB and EB spectra for the 2018 *Planck* 353 GHz data for comparison with the empirical models. The magenta line shown in each panel represents the approximate TB power-law fit found by Planck Collaboration XI (2018) for their LR71 mask. Although we show a small number of sample models, finding realizations which produce a consistently positive TB power spectrum is not difficult. The two models that used data-based polarization angle maps consistently show a positive TB signal. Our results suggest that the TB signal is likely a real feature of the Milky Way polarization structure.

plitude A^{TB} is not directly tabulated, but can be computed from the product of the EE amplitude and mean TE/EE amplitude ratios in their Table 1, multiplied by the quoted TB/TE power ratio of ~ 0.1 . The magenta line serves as a fiducial when comparing with the other three model spectra.

The remaining panels in Figure 5 illustrate the effect on TB and EB of varying the polarization fraction and angle between extremes in complexity (simple vs. data). EB is little affected except for variations at low multipoles. A positive TB signal approaching observed levels (represented by the same magenta line) is present only when

a polarization angle γ based on 353 GHz data is used. Thus a γ with more complex spatial structure than that of the simple GMF model is required to produce non-zero TB , although this does not indicate what particular property of γ is the cause.

Planck Collaboration XI (2018) note that current understanding of instrument polarization angle measurement errors preclude a simple rotational angle error as the cause of the positive TB signal. Additionally, a simple rotational angle error should also leak into the EB spectrum, which is not observed. Since it is apparent that γ is the crucial factor in producing non-zero TB , we

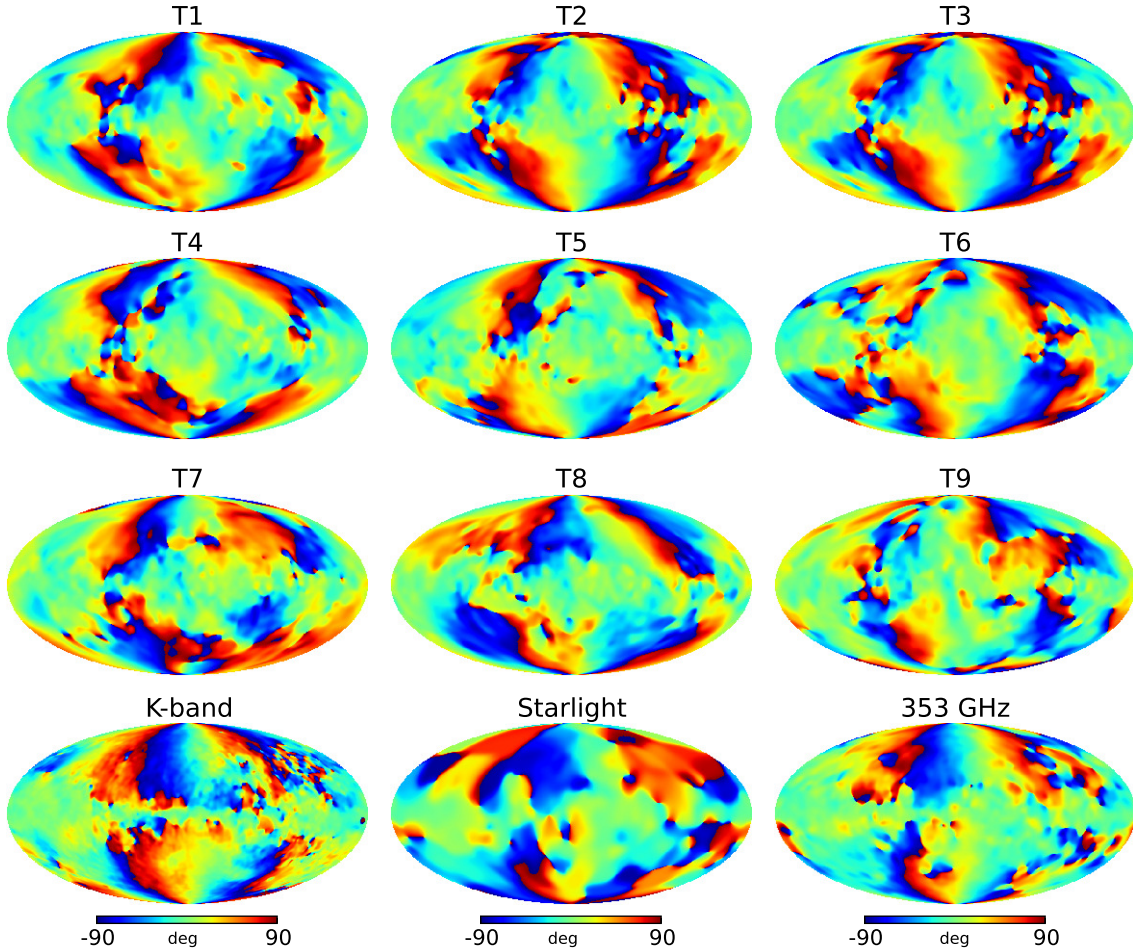


Figure 7. Polarization angles used in forming the maps that produced the twelve TB and EB power spectra shown in Figure 6. A non-zero TB spectrum can result from polarization angle morphologies which are visually different from that of the 353 GHz data. In Figure 6, four of the eleven empirical models showed a positive TB signal. Two of these are taken from data (‘K-band’ and ‘Starlight’) and strongly correlate with the 353 GHz γ morphology. However, realizations T6 and T9 from the TIGRESS simulations bear little resemblance to the 353 γ and yet produce non-zero TB .

explore additional simple models of Q and U in which we fix I and f components to match *Planck* 353 GHz observations, but substitute in a variety of simulated and data-based maps of γ that are derived independently of the *Planck* observations. This allows us to evaluate how easily one may obtain TB and EB dust spectra which are similar to those observed by *Planck* at 353 GHz, but are not affected by possible residual systematics in the *Planck* dust polarization angle.

Simulated Q and U maps of polarized dust emission have recently been made public⁶ by Kim et al. (2019). These “TIGRESS sims” provide a suite of polarized dust maps for nine observer positions within the solar neighborhood covering multiple evolutionary time-steps and are generated numerically using a multiphase, turbulent, magnetized interstellar medium (MHD code and TIGRESS ISM framework). We create nine simulated polarization angle maps from smoothed versions of the Q and U realizations for the nine observer positions and the $t = 360$ Myr time-step in their several-hundred Myr evolutionary interval. In addition to these nine realizations, we include two representations of polarization an-

gle based on data. The first of these is the *WMAP* K-band polarization angle, which actually represents synchrotron emission, but has some similarities to the dust polarization angle because both emission components are influenced by the same global magnetic field. For our second data-oriented polarization angle map, we adopt the polarization angle constructed from the *WMAP* dust polarization templates⁷. This angle is derived from observations of the optical polarization of starlight by dust grains (Page et al. 2007), which may be expected to have some similarities to the dust polarization angle at 353 GHz, although more sparsely sampled over the sky. None of the eleven discussed options are available at high spatial resolution. We replicate the pixels in Q and U maps to create maps pixelized at HEALPix $N_{\text{side}} = 2048$, but then smooth to 5° FWHM resolution and compute the γ map from the smoothed Q and U maps. Thus all eleven of the γ map realizations used in our models possess information only on 5° scales or larger, but the I and f components of the models provide small-scale structure.

Figure 6 shows the TB and EB spectra computed from the 11 models of Q and U sky maps we constructed using

⁶ https://lambda.gsfc.nasa.gov/simulation/tb_tigress_data.cfm

⁷ https://lambda.gsfc.nasa.gov/product/map/dr5/templates_info.cfm

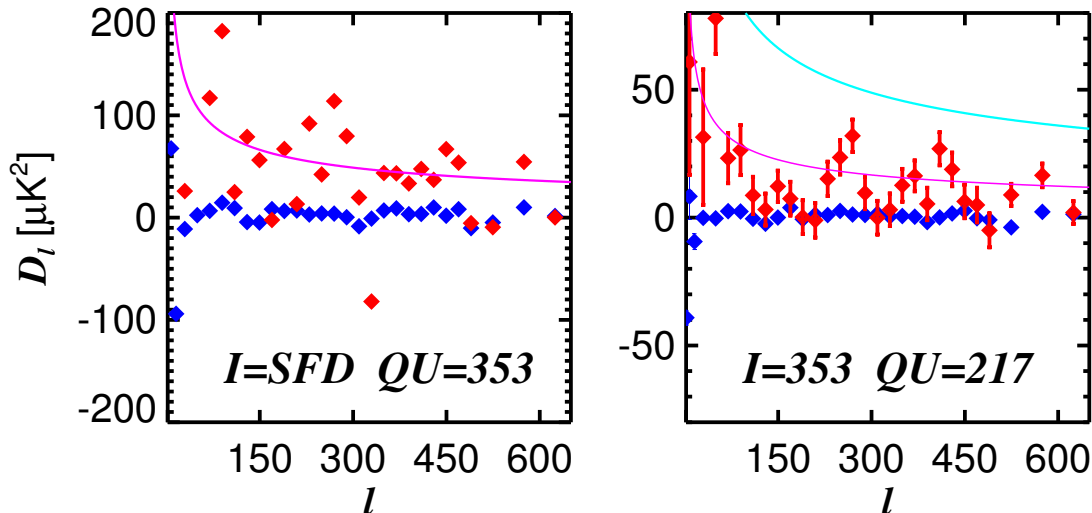


Figure 8. *Left:* Binned TB (red) and EB (blue) power spectra computed over the 75% sky region for a simulation in which $[Q, U]$ are the *Planck* 353 GHz maps, but I is derived from the [Schlegel et al. \(1998\)](#) dust intensity model evaluated at the effective frequency of the 353 GHz band. There should be no common-mode systematics between the I model and the 353 GHz data, yet a TB spectrum similar to that computed using only 353 GHz data (magenta line) results. *Right:* TB and EB cross power spectra computed from *Planck* 353 GHz half-mission 1 I and 217 GHz half-mission 2 $[Q, U]$ maps. The cyan line represents the published 353x353 TB power spectrum; the magenta line is not a fit to the 217x353 spectrum but an extrapolation of the cyan line assuming a modified black body emission law. The 217x353 uncertainties are evaluated using the *Planck* FFP10 simulations. These tests support the idea that the 353 GHz positive TB spectrum arises from Galactic emission properties.

the polarization angles described above. We use the same 75% sky mask described at the beginning of this section. Spectra are labeled according to the choice of γ , since I and f are the same for all realizations, with “T1-T9” in the first three rows referring to the nine TIGRESS simulations, and the last row showing the K-band and starlight polarization associated models, with the lower corner illustrating the 353 GHz data spectra (shown in Figure 5 with error bars) for comparison. Among the 11 models, there is a wide variation in TB spectrum amplitude with the choice of polarization angle map. Of the nine realizations that use the TIGRESS-derived polarization angle, two (observers 6, 9) show TB spectra consistently above zero, and one (observer 2) is consistently below zero. The two models that use data-based γ components both show a positive TB spectrum. Although these latter two appear on visual inspection to strongly correlate with the 353 GHz polarization angle, the γ maps corresponding to observers 6 and 9 (Figure 7) do not. Although not shown, we also evaluated TB and EB for an additional nine TIGRESS-based models using the maps from the last time-step in their evolutionary sequence. In this case, three of the nine TB spectra showed non-zero TB signals.

It therefore appears not to be difficult to generate non-zero TB Galactic dust maps from simulations of the polarization angle constructed using current GMF models, and non-zero TB seems robust to substitutions of γ from other observational data. We also note that spatial variations in polarization angle need not be small-scale to produce a positive TB signature, since the γ maps here contain variations on 5° scales or larger.

5. ADDITIONAL TESTS OF TB SIGNAL PERSISTENCE

If non-zero TB is a property of Galactic emission, then it is reasonable to expect the effect not to be confined to 353 GHz, nor to one specific mask. In this section, we briefly examine varying combinations of maps and masks

that test for persistence of the TB correlation.

[Planck Collaboration XI \(2018\)](#) computed 353 GHz half-mission TB and EB cross-spectra for six nested masks constructed based on dust emission intensity thresholds. The masks admitted between 26 - 71% of the sky for analysis. They found TB power law amplitudes that decreased with sky fraction, but were still consistent with a non-zero TB signal. Rather than basing mask generation on dust intensity thresholds, we used the FFP10 noise simulations to derive masks in which polarized noise contributions from the large-scale instrument systematics were lowest. Our smallest mask admitted $\sim 22\%$ of the sky for analysis, in two regions very roughly approximating caps about the ecliptic poles. This is a test that can only be performed for 353 GHz data because of signal-to-noise constraints, but we still found evidence for persistence of a non-zero TB signal when using this masking set.

We next compute TB power spectra for cases in which the 353 GHz polarization maps are retained, but the intensity map is adopted from observations other than the *Planck* 353 GHz I maps. The use of an alternate I map is designed to avoid possible leakage of instrument systematics between the intensity and polarization maps. We tried combinations including *Planck* 545 and 857 GHz intensity maps scaled to 353 GHz emission levels and the *Planck* dust intensity amplitude map derived from Commander multi-frequency analysis [Planck Collaboration X \(2016\)](#), but still recovered the TB correlation at observed levels. Because it is possible that there is some common-mode systematic between all *Planck* HFI frequencies, we also evaluated a model for the 353 GHz dust intensity ([Schlegel et al. 1998](#), SFD dust model 8). Although an older model, the SFD intensity map is based on IRAS and COBE/DIRBE data that are completely independent of any *Planck* observations. The TB spectrum obtained from the SFD intensity map and 353 GHz $[Q, U]$ maps is shown in the left panel of Figure 8. This

recovered TB spectrum is similar to that for the 353 GHz data, as shown by the magenta line.

Finally, we attempted to examine dust polarization data from additional frequencies. This is a test of limited scope, because currently only *Planck* data provide the necessary sky coverage, and dust signal-to-noise is decreasing at the next available frequency of 217 GHz. Additionally, TB computation using only 217 GHz intensity and polarization data does not produce a significant result in part because the 217 GHz I dust signal is diluted by CMB at higher latitudes. We instead evaluate TB for the 75% sky region using the 353 GHz half-mission 1 I map and 217 GHz half-mission 2 $[Q, U]$ maps, shown in the right panel of Figure 8. In this panel, the cyan curve is the 353 GHz TB power-law described previously. The magenta line is the extrapolation of the observed 353 GHz TB signal assuming the amplitude of the polarized dust emission follows a modified black body emission law described by a single physical dust temperature $T_d = 20K$ and spectral index $\beta_d = 1.6$. There are more data points below the magenta line than above, so that the extrapolation is not an exact predictor of the result. However, data points for the 217x353 TB spectrum predominantly lie above zero, providing additional evidence for positive TB persistence beyond 353 GHz.

6. CONCLUSIONS

We have explored the basic morphology of E and B maps of Galactic dust emission and have used intensity, polarization fraction and polarization angle components to build simple empirical models of the dust emission. We computed TB and EB power spectra for these models and investigated how I , f and γ contribute to TB . We find that:

1. Contributions to dust polarization map morphology from intensity (I), polarization angle (γ) and polarization fraction (f) components are more easily distinguished in the E and B maps than Q and U . The E component is strongly dependent on the large angular scale polarization angle structure, reflecting the GMF orientation. Large-scale dust B -mode structure takes the form of a quadrupole about the local arm viewing directions near $l = 65^\circ$ and 240° , and expresses itself as a strong $l = 3, |m| = 3$ B -mode pattern about the Galactic plane. The exact morphology of the $l = 3$ mode is constrained by the dust polarization fraction.
2. Polarization angle is the key component in producing the observed *Planck* 353 GHz non-zero TB spectrum.
3. Intensity and polarization fraction maps with small scale structure ($l > 600$), combined with large angular scale ($> 5^\circ$) polarization angle morphology, are capable of producing a non-zero TB spectrum similar to that of the *Planck* PR3 353 GHz data.
4. Within the context of our empirical models, we use a small sample of polarization angle realizations taken from the TIGRESS simulations to show that a non-zero TB spectrum is a property of individual realizations. This implies a geometrical or spatial

origin rather than a need for physics beyond that already incorporated in codes such as TIGRESS. Polarization angle maps derived from observational data independent of *Planck* (WMAP K-band, dust polarization of starlight) also produce a non-zero TB spectrum.

5. The observed non-zero TB spectrum is persistent with variations of masking and alternate choices for the intensity map, including a dust intensity model completely independent of *Planck* observations. We find additional evidence for persistence of non-zero TB computed from 353 GHz I and 217 GHz $[Q, U]$ maps.

We have substituted estimates of I , f and γ components within our empirical models that are independent of the *Planck* 353 GHz observations and found realizations for which non-zero TB persists. Our findings support the conclusion that the *Planck* 353 GHz non-zero TB spectrum is a physical property of Galactic dust polarization. In light of our studies in the paper, observing non-zero TB due to the Galactic dust foreground is not unusual or surprising. It will be interesting to see if future experiments with higher sensitivity detect non-zero EB .

This research was supported in part by NASA grants NNX16AF28G, NNX17AF34G, 80NSSC19K0526 and by the Canadian Institute for Advanced Research (CIFAR). This research has made use of NASA's Astrophysics Data System Bibliographic Services. Some of the results in this paper have been derived using the *healpy* and *HEALPix* package. We acknowledge the use of the Legacy Archive for Microwave Background Data Analysis (LAMBDA), part of the High Energy Astrophysics Science Archive Center (HEASARC). HEASARC/LAMBDA is a service of the Astrophysics Science Division at the NASA Goddard Space Flight Center. We also acknowledge use of the *Planck* Legacy Archive. *Planck* is an ESA science mission with instruments and contributions directly funded by ESA Member States, NASA, and Canada.

REFERENCES

- Ade, P., Aguirre, J., Ahmed, Z., et al. 2019, *Journal of Cosmology and Astro-Particle Physics*, 2019, 056
- Allison, R., Caucal, P., Calabrese, E., Dunkley, J., & Louis, T. 2015, *Phys. Rev. D*, 92, 123535
- Bennett, C. L., Larson, D., Weiland, J. L., et al. 2013, *ApJS*, 208, 20
- Benson, B. A., Ade, P. A. R., Ahmed, Z., et al. 2014, in *Society of Photo-Optical Instrumentation Engineers (SPIE) Conference Series*, Vol. 9153, *Millimeter, Submillimeter, and Far-Infrared Detectors and Instrumentation for Astronomy VII*, 91531P
- Chon, G., Challinor, A., Prunet, S., Hivon, E., & Szapudi, I. 2004, *MNRAS*, 350, 914
- Górski, K. M., Hivon, E., Banday, A. J., et al. 2005, *ApJ*, 622, 759
- Heiles, C. 2000, *AJ*, 119, 923
- Henderson, S. W., Allison, R., Austermann, J., et al. 2016, *Journal of Low Temperature Physics*, 184, 772
- Hu, W., & White, M. 1997, *New A*, 2, 323

- Huffenberger, K. M., Rotti, A., & Collins, D. C. 2019, arXiv e-prints, arXiv:1906.10052
- Kamionkowski, M., Kosowsky, A., & Stebbins, A. 1997, Phys. Rev. D, 55, 7368
- Kaufman, J. P., Miller, N. J., Shimon, M., et al. 2014, Phys. Rev. D, 89, 062006
- Kim, C.-G., Choi, S. K., & Flauger, R. 2019, arXiv e-prints, arXiv:1901.07079
- Koopman, B., Ausermann, J., Cho, H.-M., et al. 2016, in Society of Photo-Optical Instrumentation Engineers (SPIE) Conference Series, Vol. 9914, Millimeter, Submillimeter, and Far-Infrared Detectors and Instrumentation for Astronomy VIII, 99142T
- Page, L., Hinshaw, G., Komatsu, E., et al. 2007, ApJS, 170, 335
- Planck Collaboration Int. LIV. 2018, arXiv e-prints, arXiv:1801.04945
- Planck Collaboration Int. XXX. 2016, A&A, 586, A133
- Planck Collaboration IV. 2018, arXiv e-prints, arXiv:1807.06208
- Planck Collaboration X. 2016, A&A, 594, A10
- Planck Collaboration XI. 2018, arXiv e-prints, arXiv:1801.04945
- Planck Collaboration XII. 2018, arXiv e-prints, arXiv:1807.06212
- Schlegel, D. J., Finkbeiner, D. P., & Davis, M. 1998, ApJ, 500, 525
- Szapudi, I., Prunet, S., Pogosyan, D., Szalay, A. S., & Bond, J. R. 2001, ApJL, 548, L115
- Zaldarriaga, M., & Seljak, U. 1997, Phys. Rev. D, 55, 1830
- Zonca, A., Singer, L., Lenz, D., et al. 2019, Journal of Open Source Software, 4, 1298.
- <https://doi.org/10.21105/joss.01298>